

Cohesive laws describing the interface behaviour of iron/precipitate interfaces under mixed loading conditions

Elzas, Astrid; Thijsse, Barend

DOI

[10.1016/j.mechmat.2018.10.010](https://doi.org/10.1016/j.mechmat.2018.10.010)

Publication date

2019

Document Version

Accepted author manuscript

Published in

Mechanics of Materials

Citation (APA)

Elzas, A., & Thijsse, B. (2019). Cohesive laws describing the interface behaviour of iron/precipitate interfaces under mixed loading conditions. *Mechanics of Materials*, 129, 265-278.
<https://doi.org/10.1016/j.mechmat.2018.10.010>

Important note

To cite this publication, please use the final published version (if applicable).
Please check the document version above.

Copyright

Other than for strictly personal use, it is not permitted to download, forward or distribute the text or part of it, without the consent of the author(s) and/or copyright holder(s), unless the work is under an open content license such as Creative Commons.

Takedown policy

Please contact us and provide details if you believe this document breaches copyrights.
We will remove access to the work immediately and investigate your claim.

Cohesive laws describing the interface behaviour of iron/precipitate interfaces under mixed loading conditions

Astrid Elzas^{a,*}, Barend Thijsse^a

^a*Delft University of Technology, Department of Materials Science and Engineering, Mekelweg 2, 2628 CD Delft, The Netherlands*

Abstract

The behaviour of 11 differently oriented iron-precipitate interfaces under mixed loading conditions is studied with molecular dynamics simulations. We find that the interface structure and the change in this structure play a key role in the response to the loading. The structure change is influenced by both the loading history and the loading direction. Depending on the interface and the loading direction, the presence of a dislocation at the interface may have an additional influence on the structure change. We update our previously derived cohesive laws for pure shear and pure tensile loading to take into account the influence of the other loading direction on the behaviour during mixed loading conditions. However, not for every interface a unique relation exists between the separations at the interface and the tractions. In those cases our cohesive laws give no exact prediction, but rather a range of possible values. The cohesive laws are intended to be used in numerical methods at the next larger length scale, such as discrete dislocation plasticity.

Keywords: Dislocations, Molecular Dynamics, Mixed Mode loading, Iron/precipitate interface, Cohesive law

1. Introduction

In everyday use, interfaces in metallic microstructures are routinely subjected to stresses. Deformation and in certain cases mechanical failure are sometimes the ultimate results. Dislocations play an important role in this, but the stress response at interfaces between grains is equally important. Advanced high strength steels show limited ductility due to interface decohesion. To correctly model the

*Corresponding author

Email address: astridelzas@gmail.com (Astrid Elzas)

material behaviour, so that the limited ductility can be explained, it is crucial to understand the interface behaviour under different loading conditions.

In this paper we describe the interface behaviour of iron-precipitate interfaces under mixed loading, elaborating on our previous studies of normal and shear loading. Not only is the interface behaviour described in detail, also cohesive laws are derived describing the behaviour under various forms of mixed loading. These cohesive laws can be used in numerical methods at the next larger length scale beyond atomic, such as discrete dislocation plasticity where interfaces are modelled by cohesive zone models.

Cohesive zone models were introduced by Barenblatt [1] and Dugdale [2] to avoid the unrealistic stress singularity at the crack tip in classical fracture mechanics. Fracture is addressed as a gradual process, where it is assumed that no stress is transmitted between the fully separated crack surfaces, while a cohesive zone ahead of the crack continues to transmit forces between a pair of virtual surfaces. A traction-crack opening displacement constitutive law governs this behaviour.

Cohesive laws can either be coupled or uncoupled, and potential-based or non-potential-based. In an uncoupled cohesive law the normal traction is independent of the tangential crack opening, while the tangential traction is independent of the normal crack opening. This is appropriate when the debonding process occurs for one mode or is largely dominated by it. In coupled cohesive laws both the normal and the tangential tractions depend on the normal and tangential separations.

In a potential-based cohesive law the first derivatives of an interface potential function give the traction-separation relations. The most commonly implemented cohesive zone model is the model developed by Xu and Needleman [3] based on the potential ϕ :

$$\phi(u_n, u_t) = \phi_n + \phi_n \exp\left(-\frac{u_n}{\delta_n}\right) \left[\left\{1 - r + \frac{u_n}{\delta_n}\right\} \left(\frac{1-q}{r-1}\right) - \left\{q + \left(\frac{r-q}{r-1}\right) \frac{u_n}{\delta_n}\right\} \exp\left(-\frac{u_t^2}{\delta_t^2}\right) \right], \quad (1)$$

where u_n and u_t are the normal and tangential separation across the interface, δ_n and δ_t are interface-characteristic length parameters, and q and r are coupling parameters that couple the normal and tangential behaviour,

$$q = \frac{\phi_t}{\phi_n}, \quad (2)$$

where ϕ_t is the work of tangential separation and ϕ_n is the work of normal separation, and

$$r = \frac{u_n^*}{\delta_n}, \quad (3)$$

where u_n^* is the normal separation after complete shear separation under zero normal traction.

The normal and tangential tractions are obtained by differentiating Equation 1 with respect to u_n , respectively u_t , giving unique relations for $T_n(u_n, u_t)$ and $T_t(u_n, u_t)$. This cohesive zone model allows for shear-failure, since the tangential response is not periodic.

In order for this model to describe physically realistic interface behaviour the normal and tangential behaviour should be adequately coupled. Van den Bosch *et al.* [4] showed that only for $r = q$ the required tangential traction increases with increasing normal compression, as it does in friction. Furthermore, physical realistic coupling is obtained only for $q = 1$, since only then the required normal traction reduces to zero at complete shear separation. However, this implies that $\phi_t = \phi_n$, which experimental studies [5] have shown is often not true. Van den Bosch *et al.* [4] modified the Xu-Needleman cohesive zone model by allowing for $\phi_n \neq \phi_t$. This model is no longer potential-based.

Other cohesive zone models were developed by Park *et al.* [6], McGarry *et al.* [7], and Dimitri *et al.* [8], as we described in a previous work [9].

Conventionally the parameters for a traction-separation law are obtained empirically, from polycrystalline samples. However, in that case they reflect the average response of many interfaces. This is therefore inappropriate as a representation of constitutive behaviour of interfacial debonding at the nano-scale. To obtain the parameters of the cohesive law for accurately describing interfacial debonding at the nano-scale, atomistic simulations can be used.

As described in [9], various studies have been performed to determine cohesive zone law parameters with molecular dynamics (MD) simulations, such as [10, 11, 12, 13, 14, 15, 16, 17, 18]. However, none of these studies describe iron-precipitate interfaces under mixed loading conditions.

In a previous study we used MD to derive a cohesive law for pure normal loading for various iron-precipitate interfaces, assuming that the separations parallel to the interface are zero, which gives the relation between traction and separation during crack growth based on a universal adhesive energy equation [19]. In this study we used a model material X for the precipitate. Material properties of X will be given later on. To derive the universal adhesive energy relation, both the normal separation and the adhesive energy are scaled, according to

$$u^* = \frac{u_n}{\alpha}, \quad (4)$$

where α is the equilibrium pair interaction length between Fe and X as given by the Fe – X pair potential, and

$$E_{ad}^*(u^*) = E_{ad}/\Delta E, \quad (5)$$

where ΔE is the absolute value of the minimum adhesive energy. The universal adhesive energy relation is then given by

$$E_{ad}^* = - (1 + \theta u^* + \mu(\theta u^*)^3) \exp(-\theta u^*), \quad (6)$$

with parameter values that we found to be $\theta = 5.29$ and $\mu = -0.06$. From this universal adhesive energy relation the cohesive law describing the relation between normal traction and normal separation is derived as

$$T_n(u_n) = c\Delta E \frac{\theta^2}{\alpha^2} \left(\mu \left(\frac{\theta}{\alpha} \right)^2 \left(\frac{u_n}{c} \right)^3 - 3\mu \frac{\theta}{\alpha} \left(\frac{u_n}{c} \right)^2 + \frac{u_n}{c} \right) \exp\left(-\theta \frac{u_n}{c\alpha}\right), \quad (7)$$

where c is a scaling factor, which is material (combination) dependent, to take into account atomic strains and rearrangements. For the Fe – X interfaces $c = 2.39$.

Previously we also derived a cohesive law to describe the response to a pure shear load for the same iron-precipitate interfaces [9]. Under a shear load these interfaces showed interface sliding. The relation between tangential traction and tangential separation depends on the interface structure and the loading direction. In [9] we found that a cohesive law describing the relation between tangential traction and tangential separation should be described in three parts: an elastic part for small separations, a steady-state sliding part for large separations, and a transition part in between, where the steady-state sliding behaviour develops. This cohesive law is given by

$$\begin{aligned} T_t &= \frac{T_t^{crit}}{u_t^{crit}} u_t, & \text{for } 0 \leq u_t \leq u_t^{crit}, \\ T_t &= \frac{T_t^{crit} - T_t^s}{(u_t^s - u_t^{crit})^2} (u_t - u_t^s)^2 + T_t^s, & \text{for } u_t^{crit} \leq u_t \leq u_t^s, \\ T_t &= T_t^s, & \text{for } u_t \geq u_t^s, \end{aligned} \quad (8)$$

where u_t^{crit} is the separation at which the structure starts to slide and T_t^{crit} is the corresponding value of the traction; u_t^s is the separation at which steady-state sliding behaviour is reached and T_t^s is the corresponding sliding traction.

When a dislocation impinges on the interface when the system is subjected to a shear load, the dislocation might trigger a structure change of the interface from the impingement position onwards. In this case the cohesive law relating tangential traction to tangential separation should be modified to take this gradual structure change into account. The modified cohesive law is given by

$$T_t = (1 - \xi) T_t^{orig} + \xi T_t^{new}, \quad (9)$$

where T_t^{orig} is the original cohesive law for the unchanged interface and T_t^{new} is the cohesive law for the changed part of the interface. The time dependent parameter ξ expresses the progress of the change of the interface,

$$\xi = \frac{A_{new}}{A_{orig} + A_{new}}, \quad (10)$$

where A_{orig} is the area of the interface that still has the original structure and A_{new} is the area that has the changed structure.

In the present study we analyse the influence of mixed loading conditions on the relation between tractions and separations at the interface, since it is expected that a combination of normal and tangential loading will influence the relations for pure normal and pure tangential loading as given in Equations 7 and 8. In section 2 the choice of material, the set-up of the simulation, and the analysis methods are described. The influence of a previously applied normal load on the relation between tangential traction and tangential separation during shear loading, here called 'pre-tension' loading, is described in section 3.1. The influence of a previously applied shear load on the relation between normal traction and normal separation during normal loading, here called 'pre-shear' loading, is described in section 3.2. The response of the interfaces to a simultaneously applied normal and shear load, so called mixed-mode loading, is described in section 3.3. In section 4 the previously derived cohesive laws for pure normal and pure shear loading are adjusted to include the influence of the other loading direction under pre-shear, pre-tension and mixed-mode loading. The results are discussed in section 5. Finally, in section 6 the conclusions are drawn.

2. Method

2.1. Material description

In this study the same iron-precipitate interfaces as in [19] and [9] are studied, but here under different loading conditions. Iron is described with the EAM-potential by Ackland *et al.* [20]. In the EAM format the potential energy of atom i is given by

$$U_i = F(\rho_i) + 1/2 \sum_j \phi_{ij}(r), \quad (11)$$

where F is the embedding energy of atom Fe or atom X as a function of the local electron density ρ_i , and ϕ_{ij} is the pair interaction between atom i and the surrounding atoms j as a function of their distance r . The local electron density ρ_i is made up from the contributions ψ_j to the electron density by the same atoms

j surrounding atom i at distances r ,

$$\rho_i = \sum_j \psi_j(r). \quad (12)$$

F , ϕ and ψ are relatively simple functions, parametrised for Fe. They can be found in the original paper [20]. The artificial precipitate material X is chosen to be material X⁽³⁾ from [21]. Material X has a 10 % larger lattice constant than Fe and, as a result of the X – X pair interaction being twice as strong as that of Fe – Fe and the X- and Fe-embedding terms being equal, X has a 49 % larger Young’s modulus than Fe. Material X is thus stiffer than Fe and, due to the different lattice constant, forms semi- or non-coherent interfaces with Fe. Dislocation transfer into the precipitate material is therefore hindered, just as it is in real precipitate materials found in steel, such as carbides and nitrides of different alloying elements. Similar to [21], the mixed Fe – X pair interaction is a linear combination of the individual Fe – Fe and X – X pair interactions,

$$\phi_{FeX} = q(\phi_{FeFe} + \phi_{XX}), \quad (13)$$

where the factor q in this study equals 1/3. This Fe – X pair interaction in combination with the orientations of the Fe and X grains on either side of the interface determines the interface strength. However, defects at the interface, those initially present but also those developing during loading and grain sliding, may be of significant additional influence.

2.2. Setup

The Fe – X system is schematically shown in Figure 1. The system size is dependent on the orientation of the crystals, and on average equals $165 \times 4.4 \times 110$ nm³, with the number of atoms per system varying between 6 and 9 million. The system is periodic in x and y .

The orientations of the 11 different interfaces, being the same as the ones studied in [19] and [9], are listed in Table 1. Since in α -iron the typical cleavage plane is the (100) plane, with the crack front direction in either the [001] or the [011] direction, the most logical starting point for the study of interface decohesion, as is also the focus of [19], is a system with the (100) plane in the interface, which upon decohesion becomes the crack plane. To study the interaction of a dislocation with such an interface, the dislocation line has to be in a periodic direction to avoid edge effects. The choice is therefore made to study dislocations of the $\{112\}\langle 111 \rangle$ slip system, so that the dislocation line is in the [011] direction, which, with the (100) plane at the interface, is the crack front direction. With this as starting point, the orientations of the iron and precipitate crystal are varied to obtain the orientations given in Table 1. The simulations are performed with one dislocation

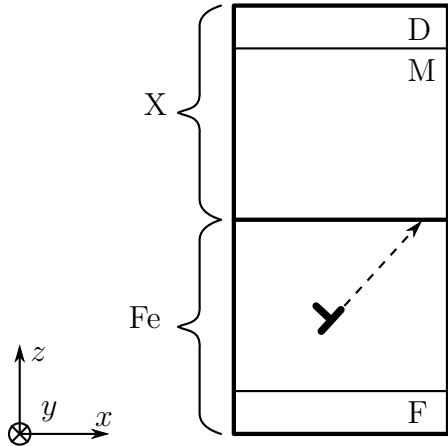


Figure 1: Setup of the simulations. The simulation box consists of an Fe – X bicrystal, which is periodic in x - and y -direction. The atoms in region F are kept fixed, atoms in region M are mobile atoms, whose positions are updated by time integration, and the atoms in region D are moved with a constant strain rate of $\dot{\epsilon} = 10^8 \text{ s}^{-1}$. In the Fe grain one $\{112\}\langle 111 \rangle$ edge dislocation is inserted close to the interface, so that upon minimisation it moves towards the interface. The X grain is the precipitate material.

present in the iron grain at the interface. The dislocation is initially placed in the iron grain at 10 \AA underneath the interface by removing a half plane of atoms. Upon energy minimisation the dislocation moves to the interface where it halts. By starting the simulations with the dislocation at the interface, instead of far below the interface, the influence of the different angles between glide plane and loading direction for the different oriented Fe grains is minimised.

In the simulations atoms in the lower 10 \AA are kept fixed, region F in Figure 1. On atoms in the upper 10 \AA , region D, a displacement is imposed so that a constant strain rate $\dot{\epsilon}$ of 10^8 s^{-1} results. For the mobile atoms, region M, time integration using a time step of 5 fs is performed at 1 K with a Nosé-Hoover thermostat. Prior to loading, the system is equilibrated at 1 K for 100 ps. The stress σ that results from the applied strain is calculated by summing the resulting forces on the atoms in region D and dividing this by the area in the x, y -plane.

The very low temperature of 1 K was chosen to be able to see details of the atomic behaviour driving the interface dynamics. At higher temperatures these details would be hidden by thermal vibrations.

The particular interface realisations for each of the 11 crystal orientations are the same as those in [19], where they were created using the method described by Tschopp and McDowell [22]. A systematic collection of interface structures was generated for each crystal orientation by energy minimisation following extremely small initial displacements in the x and y directions. Of all the possible interface structures thus generated, the structure of which the interface energy has the highest number of occurrences in the collection is chosen as the final realisation.

2.3. Local behaviour

Similar to [19], to calculate the local response to the applied load in the interface region, the region is divided into multiple bins along the x -direction. Each bin is then divided in two: one half above the interface, one half underneath, as shown

Table 1: Orientations of the Fe and X grains giving the 11 different interface structures. The angle between the dislocation glide direction and the interface is given as ζ in Fe and η in X.

		Fe			X			ζ ($^\circ$)	η ($^\circ$)
		x	y	z	x	y	z		
(100) Fe	S1	[01 $\bar{1}$]	[011]	[100]	[11 $\bar{1}$]	[011]	[21 $\bar{1}$]	35.3	0.00
	S2	[01 $\bar{1}$]	[011]	[100]	[01 $\bar{1}$]	[011]	[100]	35.3	35.3
	S3	[01 $\bar{1}$]	[011]	[100]	[$\bar{2}$ 3 $\bar{3}$]	[011]	[31 $\bar{1}$]	35.3	60.5
	S4	[01 $\bar{1}$]	[011]	[100]	[21 $\bar{1}$]	[011]	[1 $\bar{1}$ 1]	35.3	90.0
(100) X	Fe1	[111]	[011]	[21 $\bar{1}$]	[011]	[011]	[100]	0.00 ^a	35.3
	Fe3	[$\bar{2}$ 3 $\bar{3}$]	[011]	[31 $\bar{1}$]	[01 $\bar{1}$]	[011]	[100]	60.5	35.3
	Fe4	[21 $\bar{1}$]	[011]	[1 $\bar{1}$ 1]	[01 $\bar{1}$]	[011]	[100]	90.0 ^b	35.3
(110) Fe	X1	[001]	[1 $\bar{1}$ 0]	[110]	[111]	[1 $\bar{1}$ 0]	[11 $\bar{2}$]	54.7	0.00
	X2	[001]	[1 $\bar{1}$ 0]	[110]	[113]	[1 $\bar{1}$ 0]	[33 $\bar{2}$]	54.7	29.5
	X3	[001]	[1 $\bar{1}$ 0]	[110]	[001]	[1 $\bar{1}$ 0]	[110]	54.7	54.7
	X4	[001]	[1 $\bar{1}$ 0]	[110]	[$\bar{1}$ 1 $\bar{2}$]	[1 $\bar{1}$ 0]	[111]	54.7	90.0

^a The dislocation is placed in the [1 $\bar{1}$ 1] direction, giving an angle between slip plane and crack plane of 70.6 $^\circ$.

^b The dislocation is placed in the [$\bar{1}$ 11] direction, giving an angle between slip plane and crack plane of 19.4 $^\circ$.

in Figure 2. The width of each bin, δx , was chosen to be 8.8 Å, or five atomic [100] planes. The height of the bins, δz , was chosen as 20 Å. This ensures that the total interface region, which is the region in which significant extra strain is seen with respect to the bulk, is taken into account in the calculations made over each bin.

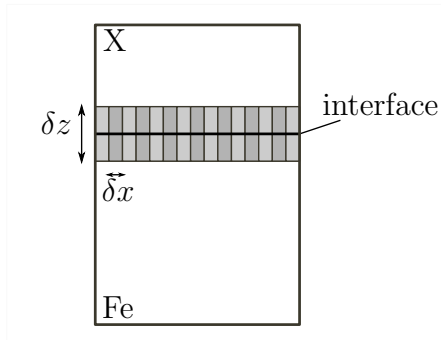


Figure 2: Division of interface region into bins with width δx of 8.8 Å and height δz of 20 Å. The bins have a role only in the data analysis, not in the simulation.

For every bin k the stress is calculated as the average of the stresses on the N_k atoms j in the bin, according to

$$\sigma_{\alpha\beta k} = \frac{1}{N_k} \sum_{j=1}^{N_k} \sigma_{\alpha\beta k j}. \quad (14)$$

The normal traction T_n in a bin is equal to the $\alpha\beta = zz$ component of this average stress in the bin and the tangential traction T_t is equal to the $\alpha\beta = xz$ component.

The normal and tangential separations u_n and u_t between the bins above and underneath the interface are calculated at the time of interest t as the increase in normal and tangential distance between the centers of mass (c) of these bins

$$\begin{aligned} u_n(t) &= z_c^X(t) - z_c^{Fe}(t) - (z_c^X(0) - z_c^{Fe}(0)), \\ u_t(t) &= x_c^X(t) - x_c^{Fe}(t) - (x_c^X(0) - x_c^{Fe}(0)), \end{aligned} \quad (15)$$

where z_c^{Fe} is the z -position and x_c^{Fe} the x -position of the center of mass of the Fe-bin, below the interface, and z_c^X is the z -position and x_c^X is the x -position of the X-bin, above the interface. For simplicity of notation, T_n , u_n , T_t and u_t do not carry a subscript designating the bin to which they apply. The values for T_n , T_t , u_n and u_t were calculated every 100 time steps (500 fs) as an average over 10 time steps (50 fs).

To determine T_t and u_t , the division of atoms into bins is made once, at the beginning of the simulation. If, under the influence of a shear load, interface sliding

occurs, the upper and lower half of the bin move apart. The increase in tangential distance between the bin halves gives u_t . However unlike the tangential case, T_n and u_n have to be determined between the upper and lower half of a bin for which the bin halves are still at roughly the same x -position. In order to determine T_n and u_n therefore, the division of atoms into bins is made every time step when these values are calculated.

As was shown in [9], in response to a shear load the individual bins do not always show equal $T_t(u_t)$ behaviour at the same moment in time. The average and the standard deviation of the response, however, is equal for all the bins. Therefore T_t can be averaged over all the bins at every desired moment in time. In addition to the $T_t(u_t)$ results for individual bins, the data are therefore also averaged over the entire interface and over time intervals of 10 ps. This averaging is done to smoothen the curves and get a better view on the similarities and differences between the different interfaces and loading directions. These average tangential traction data are indicated as $\overline{T}_t(u_t)$.

The response to a normal load is quite different for different bins at the same moment in time, as was shown in [19]. The relations between T_n and u_n of the bins are comparable, however. Therefore, instead of averaging the data of the individual bins at a particular moment in time as is done for T_t , the data for T_n of the individual bins are averaged at particular values of u_n . These average normal traction data are indicated as $\overline{T}_n(u_n)$.

2.4. Loading

Three different kinds of mixed loading conditions are applied: 1.) pre-shear: a tensile load preceded by a shear load, 2.) pre-tension: a shear load preceded by a tensile load, and 3.) mixed-mode loading: simultaneously applied tensile and shear loads. The strain rate equals 10^8 s^{-1} . For mixed-mode loading this is the total strain rate, which implies different normal and tangential strain rates under different loading angles. Under mixed-mode loading the mode-mixity angle is defined as the angle between the normal to the interface and the loading direction, so that an angle of 0° implies pure normal loading and 90° gives pure shear loading. Different mode-mixity angles ranging between 0° and 90° are studied.

2.5. Methods

The MD-simulations are performed with LAMMPS [23, 24] and the GPU-accelerated version hereof [25, 26, 27]. The structures are visualised with OVITO [28]. As a measure for changes in the interface structure the number of non-bcc atoms at the interface is determined with the common neighbour analysis as implemented in LAMMPS [29, 30]. We found this to be a sensitive diagnostic for recording structural changes at an interface.

3. Results

A schematic representation of the traction-separation relations for shear, pre-tension, mixed-mode, tension, and pre-shear loading of the different interfaces is given in Table 2. This table is intended to be a quick reference to the mechanical responses in the various situations studied. In Sections 3.1, 3.2, and 3.3 these results are discussed in detail.

3.1. Pre-tension

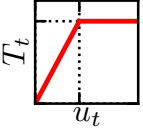
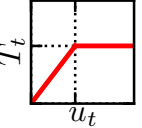
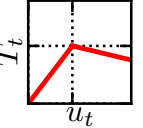
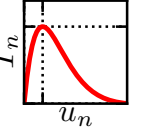
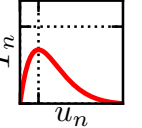
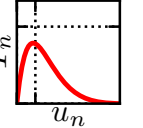
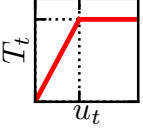
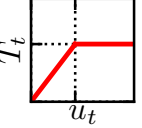
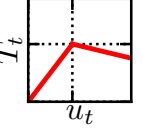
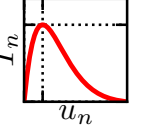
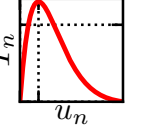
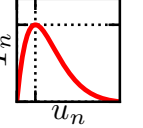
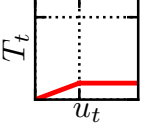
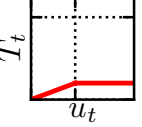
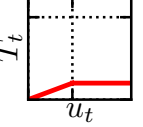
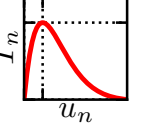
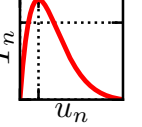
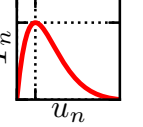
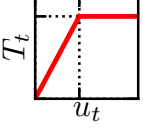
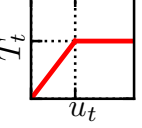
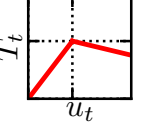
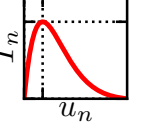
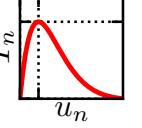
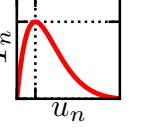
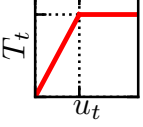
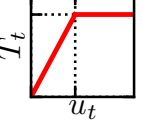
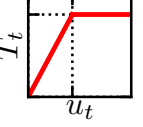
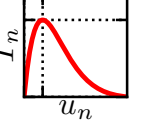
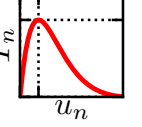
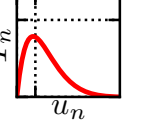
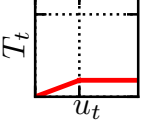
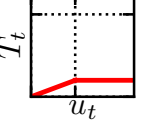
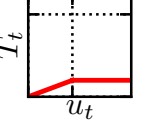
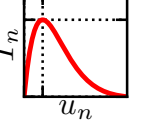
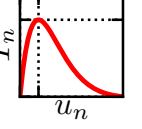
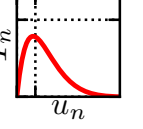
When the systems are subjected to a tensile load, the normal separation at the interface, u_n , increases. When subsequently a shear load is applied to the same system, it can be expected that the increased normal separation at the interface makes it 'easier' to shear the system, resulting in a lower tangential traction. As illustrated for the Fe4 interface in Figure 3, left, this effect is indeed seen. The longer the pre-tension time and therefore, since a constant strain rate is applied, the higher the normal strain, the lower the tangential traction is during shearing. Systems that were already 'easy' to shear without pre-tension, having a low tangential traction, stay 'easy' to shear, as illustrated for the X1 interface in Figure 3, right. The S4 interface, however, is an exception to this rule. As shown in Figure 3, middle, \overline{T}_t is not influenced by the applied pre-tension. Only after 500 ps of pre-tension, the combination of the pre-tension and the subsequent tangential loading leads to decohesion of the interface, reflected in the decreasing blue curve for 500 ps of pre-tension for $u_t > 10 \text{ \AA}$.

An overview of the influence of pre-tension on the shearing behaviour is given in Figure 4, where the sliding traction T_t^s is shown for ten interfaces after different amounts of pre-tension. A schematic representation of the influence of pre-tension on the entire traction-separation relation for shear is given in Table 2. Results for the S2 interface are not shown, since for this interface the structure dramatically changes during both pre-tension and shearing, and no steady-state sliding behaviour is reached after pre-tension. T_t^s can therefore not be determined for this interface.

3.2. Pre-shear

The response of an interface to a tensile load is proportional to its adhesive energy, as is reflected in the normal cohesive law derived in [19], Equation 7. The different interfaces result from different crystal orientations and have, as a result, different interface structures with different adhesive energies. When a shear load is applied to the systems, the structure of the entire interface changes in certain cases [9], depending on the interface and on the loading direction. It could be expected that a change in interface structure also changes the adhesive energy of the interface and with that also changes the response of such an interface to a

Table 2: Schematic representation of the response of interfaces with a dislocation initially at the interface to different loading modes. For the X1 and X2 interface an applied shear load leads to a gradual change of the interface structure from the dislocation position onwards. The response therefore will be different for larger applied shear strains.

Interfaces	Shear	Pre-tension	Mixed-mode	Tension	Pre-shear	Mixed-mode
Fe3, Fe4, S3						
Fe1						
S1						
X4						
S4						
X1, X2						

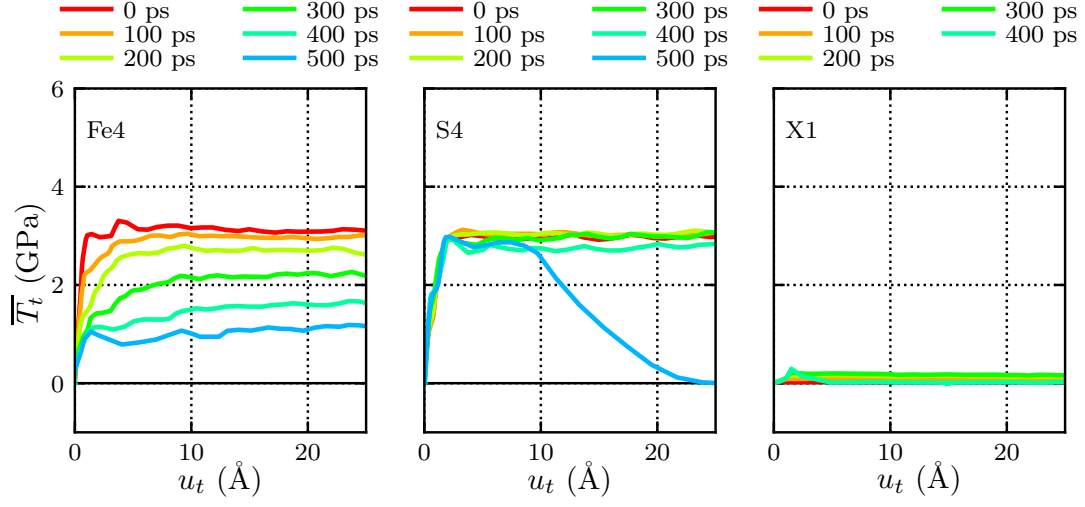


Figure 3: Tangential traction as function of tangential separation for three different interfaces after different amounts of pre-tension, indicated by the different pre-tension times, prior to loading the system in shear.

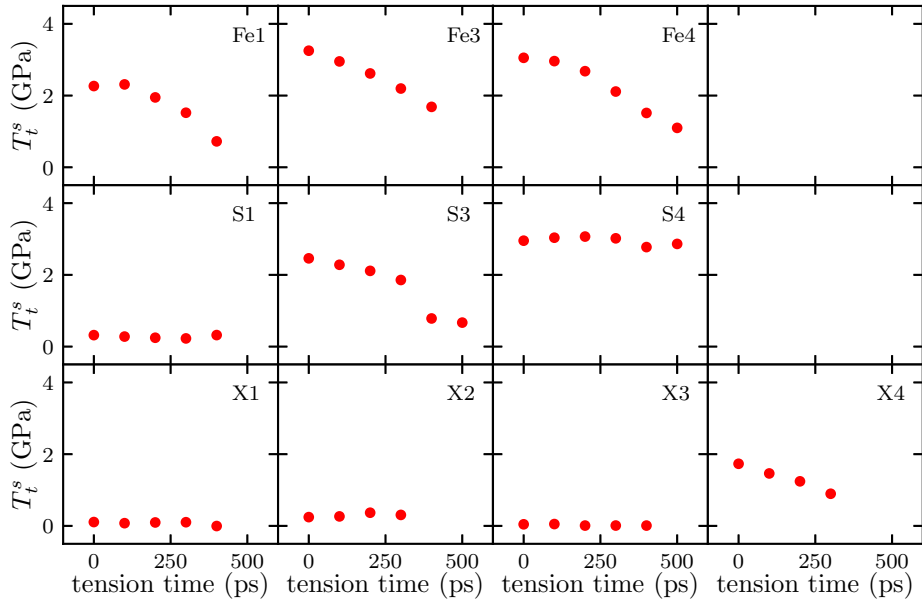


Figure 4: Sliding traction, T_t^s , during shearing as function of the pre-tension time, for ten different interfaces.

tensile load with respect to the original interface. For the Fe4 interface it is indeed seen that the pre-shear load leads to a changed normal traction during subsequent tensile loading, Figure 5.

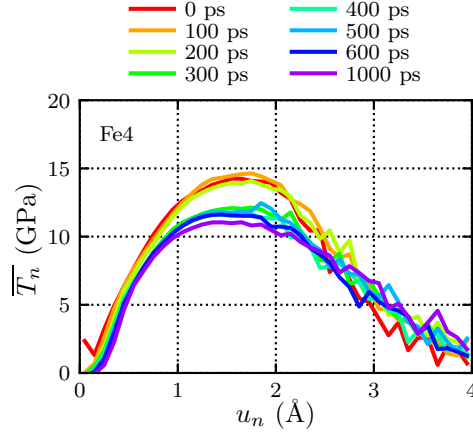


Figure 5: Normal traction as function of normal separation for the Fe4 interface under tensile loading after different amounts of pre-shear, indicated by the different pre-shear times.

The results for all interfaces are given in Figure 6, where the average of the maximum normal traction over all bins $\overline{T_n^{max}}$ is shown for nine of the interfaces after different amounts of pre-shear. A schematic representation of the influence of pre-shear on the entire traction-separation relation for tension is given in Table 2. Pre-shear can either make the system 'easier' to pull apart (Fe3, Fe4, S3), make it 'harder' (Fe1, S1), or have no significant influence (S4, X1, X2, X4). It turns out that whether or not a change in $\overline{T_n^{max}}$ is seen with increasing pre-shear time depends on whether or not the structure of the interface changes as a result of the applied shear load. So, indeed a changed interface structure leads to a different $T_n(u_n)$ relation, since the adhesive energy of the interface is also changed. For the S2 and the X3 interface no graphs are shown, because they cannot be compared to the other results: in these cases pre-shear followed by tensile loading leads to the nucleation of a dislocation loop (S2) or to the reflection of the dislocation into iron (X3). This dislocation (loop) then moves towards the lower boundary, where it is stopped by the fixed atomic planes and causes a stress concentration. From this stress concentration multiple dislocations are nucleated, leading to failing of the structure in a different way than for the other interfaces, making it impossible to compare the crack growth between the different simulations and to determine meaningful values for $\overline{T_n^{max}}$ at the interface.

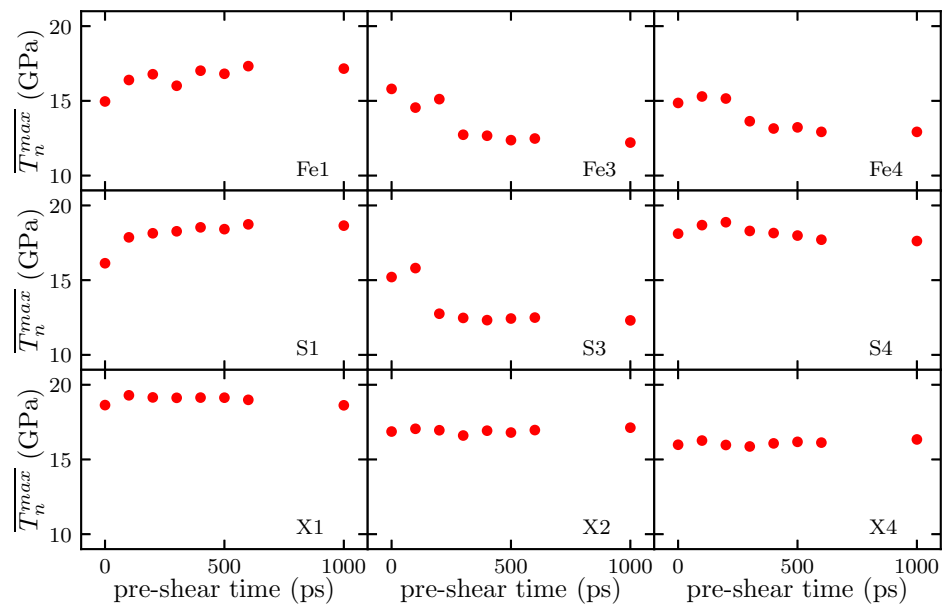


Figure 6: Average maximum normal traction during normal loading after different amounts of pre-shear are applied, indicated by the pre-shear time, for nine different interfaces.

3.3. Mixed Mode

The pre-shear and pre-tension loading conditions described in the previous sections might seem rather artificial. In practice, interfaces will be subjected to simultaneously combined shear and tensile loading, the so called mixed-mode loading. The pre-shear and pre-tension loading conditions, however, do give insight in the mechanisms that take place at the different interfaces under the different loading conditions. Based on this insight one can speculate what would happen during mixed-mode loading, as we will do in the following paragraphs.

Under mixed-mode loading conditions a combined shear and tensile load are applied to the system with a total strain rate of 10^8 s^{-1} . Based on the results for the pre-tension loading condition, Figure 4, one would expect that under mixed-mode loading a larger normal component of the load, i.e. a smaller mode-mixity angle, makes it 'easier' to shear the system for the Fe1, Fe3, Fe4, S3, and X4 interface. The normal component of the load causes u_n to increase, resulting in a smaller T_t^s . This behaviour is indeed seen, as illustrated for the Fe4 interface in Figure 7a. In contrast to the pre-tension simulations, once the system slides during mixed-mode loading the continued shearing and tensile loading lead to a continuously increasing u_n , which in turn leads to a decreasing T_t^s . This behaviour is indeed seen, as illustrated for the Fe4 interface in Figure 7a.

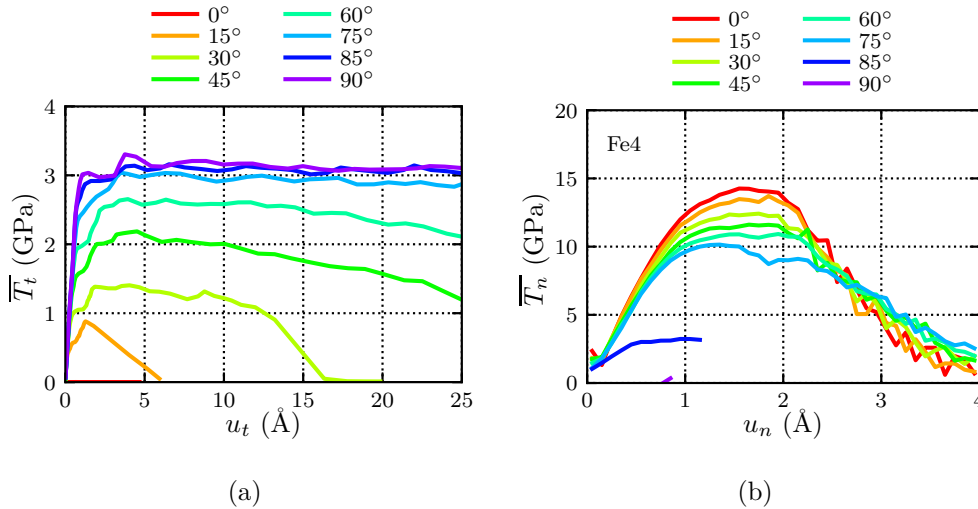


Figure 7: Fe4 interface under mixed-mode loading. Figure 7a shows that an increased normal loading component, so a smaller mode-mixity angle, leads to a decrease in $T_t(u_t)$ compared to the relation under pure shear (a mode-mixity angle of 90°). Figure 7b shows that an increased shear loading component, so a larger mode-mixity angle, leads to a decrease in $T_n(u_n)$ compared to the relation under pure normal loading (a mode-mixity angle of 0°).

Similarly as under pre-shear loading, the shear component of the mixed-mode load leads to a changing interface structure, although the change can be different

because of the simultaneously applied tensile component. The changed structure in turn influences the response to normal loading, as shown in Figure 7b. Under pre-shear loading after a certain amount of pre-shear loading a steady-state sliding regime is reached and further shear loading has no additional influence on the normal loading behaviour (Figure 5). Under mixed-mode loading however, as shown in Figure 7b, increasing the shear component leads to a gradual decrease in the normal traction for the Fe4 interface, since under mixed-mode loading the increasing shear is applied simultaneously with an increasing tensile load and therefore the interface structure gradually continues to change.

An overview of the influence of the shear component of the mixed-mode load on the normal response is given for ten of the interfaces in Figure 8. A schematic representation of the influence of mixed-mode loading on the entire traction-separation relations for shear and tension is given in Table 2. For the X3 interface no data are shown, for the same reason as given in the case of pre-shear, Section 3.2.

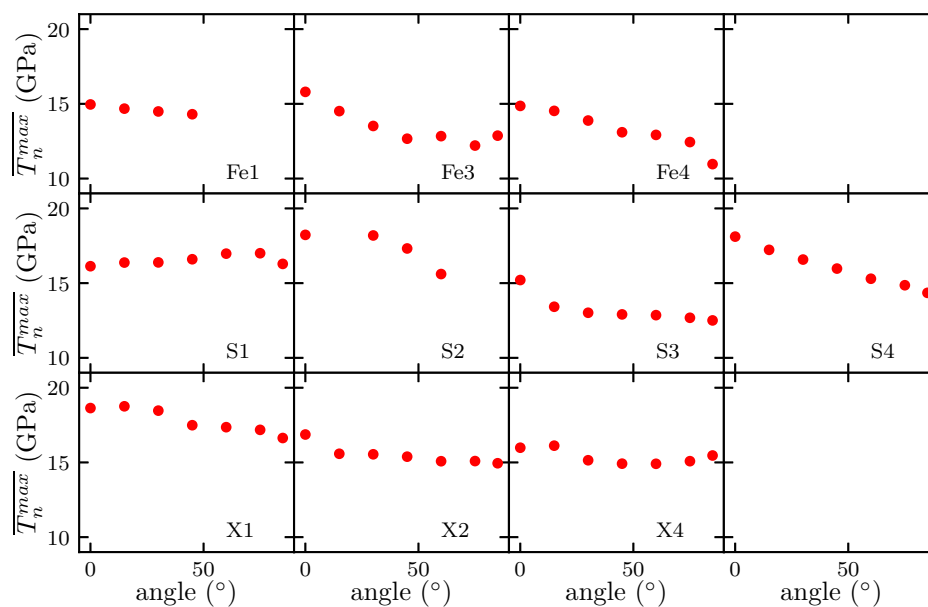


Figure 8: Average maximum normal traction during mixed-mode loading for different mode-mixity angles for ten different interfaces.

Comparing Figures 6 and 8 shows that the influence of the shear load on the normal behaviour is not for all interfaces the same under mixed-mode and pre-shear loading conditions. The third and fourth column in Table 2 further illustrate this. To compare the influence of the different loading paths on the response, in Figure

9 both \overline{T}_n and \overline{T}_t are shown as function of u_t for different values of u_n . The red dots show the values obtained with mixed-mode loading, while the blue dots result from pre-shear loading. For the Fe4 interface, as shown in Figure 9, both loading paths give similar results. In this case, therefore, u_n and u_t have the role of 'state parameters', i.e. representing the traction behaviour irrespective of the history through which the interface has evolved to these particular u_n and u_t values. In Figure 10 the influence of the different loading paths on the response are shown for the S4 interface. For this interface the different loading paths clearly give different responses, perhaps not greatly different but certainly different in a significant way.

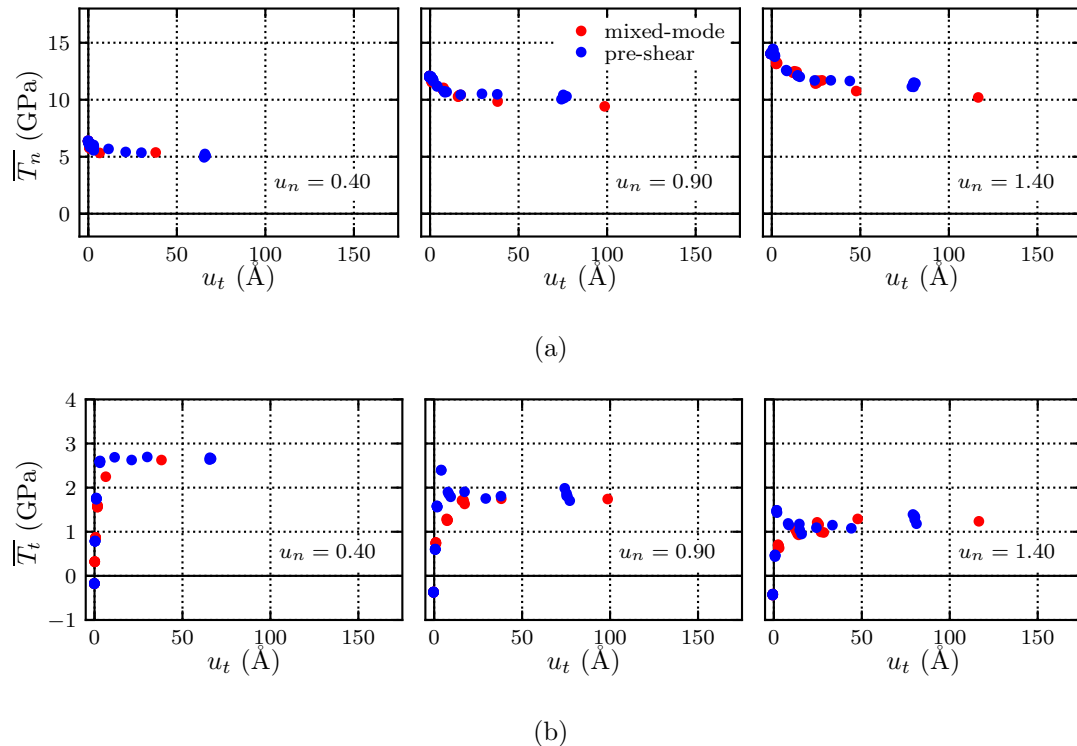
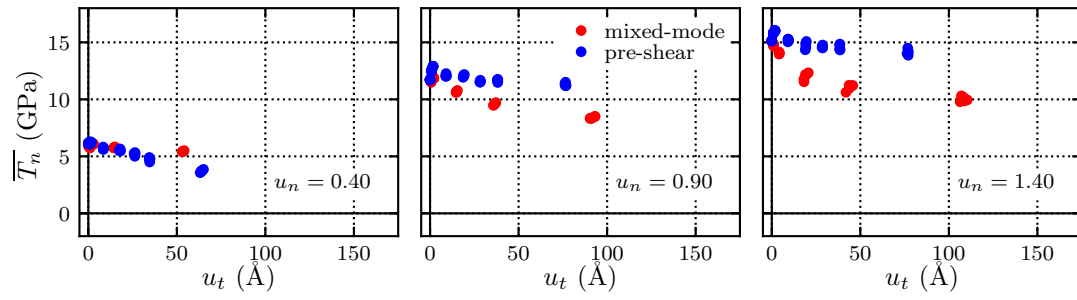


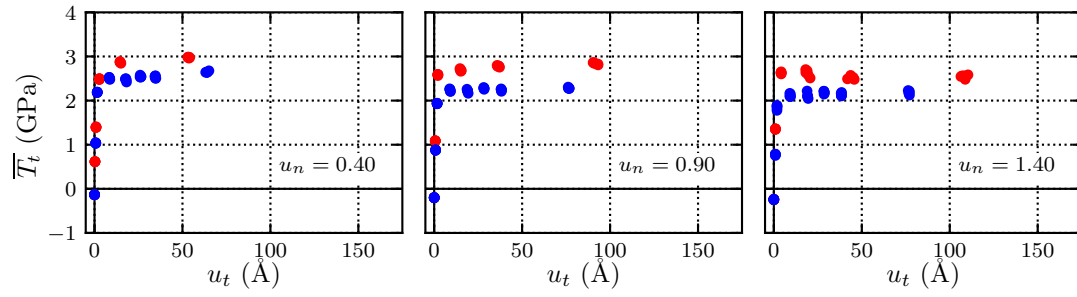
Figure 9: $\overline{T}_n(u_t)$ (a) and $\overline{T}_t(u_t)$ (b) for different values of u_n for the Fe4 interface under mixed-mode and pre-shear loading.

3.4. Structure change

The different tractions resulting from subsequently or simultaneously applied tangential and normal loading can be explained by different structure changes at the interfaces under different loading modes. As a measure for the structure change the number of non-bcc atoms per interface area is used. For the S4 interface the results for pre-shear and subsequent normal loading and for mixed-mode loading are compared in Figure 11. Note that the time in Figure 11a starts at



(a)



(b)

Figure 10: $\overline{T}_n(u_t)$ (a) and $\overline{T}_t(u_t)$ (b) for different values of u_n for the S4 interface under mixed-mode and pre-shear loading.

the beginning of the simulation and thus includes both the pre-shear and the subsequent normal loading. Under pure tension, without pre-shear (0 ps) or with a mode-mixity angle of 0° , the number of non-bcc atoms increases with time until decohesion occurs, around 600 ps, upon which n_{int} drops and becomes a constant, reflecting that the two newly formed free surfaces revert to a much more bcc-like structure. In contrast, under a (pre-)shear load n_{int} slightly increases and becomes a constant during steady-state sliding. When the normal loading starts from this new structure, the structure changes are similar for different amounts of pre-shear loading, Figure 11a, since the starting structure for normal loading is similar after every amount of pre-shear. During mixed-mode loading the combined effect of normal and tangential loading leads to different structure changes for different mode-mixity angles, as illustrated in Figure 11b, and therefore, not surprisingly, to different $\overline{T}_n(u_n)$ behaviour, as was shown in Figure 10a. For this S4 interface a larger mode-mixity angle leads to less structure change at the interface and to a lower \overline{T}_{max}^n . For the other interfaces a difference in structure change between consecutively and simultaneously applied tangential and normal loading is also found, although sometimes less pronounced than for S4.

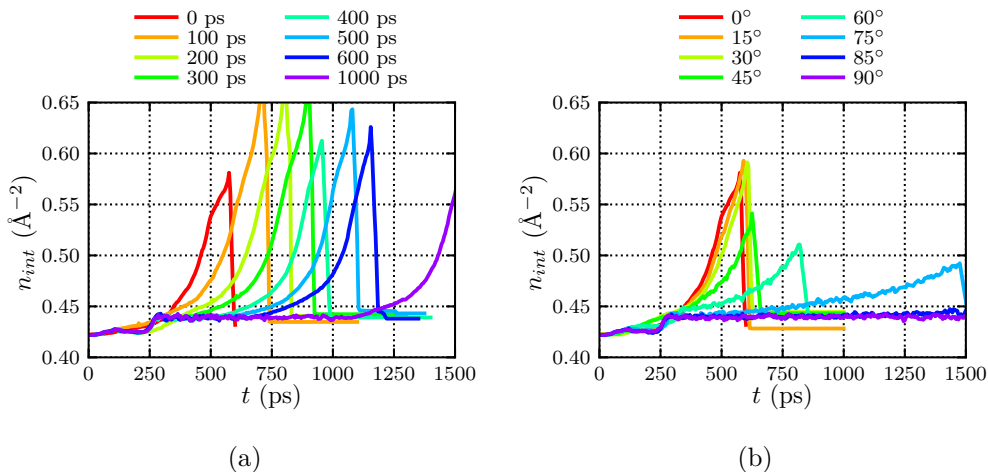


Figure 11: Change in interface structure, indicated by the number of non-bcc atoms at the interface per area as function of time, for the S4 interface during pre-shear (a) and mixed-mode (b) loading. Note that the time in (a) starts at the beginning of the simulation and thus includes both the pre-shear and the subsequent normal loading.

3.5. Other effects

In Sections 3.1 to 3.3 results are shown for the 11 studied interfaces. However, in some cases other effects are seen than only interface decohesion or interface sliding. We report this here, just to illustrate the multitude of different effects

that occur under conditions that differ only in the interface orientation. For the Fe1 interface, dislocation loops form from the interface into the iron grain under the three different loading modes but not for pure shear or pure tension. These loops coalesce and, due to the periodic boundary conditions, form a downwards moving twin plane. At the S2 interface loops are also seen to nucleate. Furthermore, under certain loading conditions a single dislocation nucleates from the interface. The dislocation initially placed at the X3 interface moves back into the iron grain under all loading conditions except pure shear. This dislocation is then blocked by the fixed atomic bottom planes, which leads to a stress concentration. From this stress concentration multiple dislocations nucleate, which in turn lead to failure of the structure in a different way than by pure interface decohesion.

Since in Sections 3.1 to 3.3 the influence of pre-shear, pre-tension or the mode-mixity angle on the tensile and shear behaviour is quantified by their effect on $\overline{T_{max}^n}$ and T_t^s , respectively, these parameters are shown only if meaningful values could be determined. However, for some interfaces the nucleated dislocations cause decohesion at multiple positions along the interface or at the boundary between fixed and dynamic atoms, which constitutes a new complication. A detailed investigation of this behaviour, however, is beyond the scope of this work.

In conclusion, the response of the interfaces to mixed-mode loading is different from the response to pre-shear or pre-tension loading. The loading direction and history determine the local stress state at the interface and with that determine the structure change that takes place at the interface. That, ultimately, influences the traction-separation behaviour.

4. Cohesive law

In [19] a cohesive law for the relation between normal traction and normal separation during crack growth under pure normal loading was derived. Although it was found that crack nucleation is influenced by impinging dislocations, since they locally modify the structure of the interface, crack growth is independent of the number of dislocations under pure normal loading. In [9] a cohesive law for the relation between tangential traction and tangential separation under pure tangential loading was derived. This cohesive law does depend on dislocations, since dislocations can change the entire interface structure and with that influence the response of the interface. In the current section the two cohesive laws are adjusted to take into account the cross effects: the influence of normal loading on the shear behaviour and that of shear loading on the normal behaviour, based on the results from the pre-shear, pre-tension, and mixed-mode simulations.

4.1. Pre-shear

The relation between normal traction and normal separation under pre-shear loading conditions can be derived from the previously derived [19] cohesive law for crack growth under pure normal loading, Equation 7, by including the influence of the shear load. If a shear load is applied to the system, the interface structure changes until a steady-state sliding regime is achieved. The largest structure change occurs until the peak of T_t is reached, as given by Equation 8. The new interface structure that forms under the applied shear load will have a different interface energy ΔE , and therefore a different relation for $T_n(u_n)$ under a subsequent normal load, than the original structure. The influence of the structure change can be included in the cohesive law by a mixing rule that describes the transition between beginning and end,

$$T_n = (1 - \zeta)T_n^{orig} + \zeta T_n^{new}, \quad (16)$$

where T_n^{orig} is $T_n(u_n)$ for the original interface structure, T_n^{new} is $T_n(u_n)$ for the changed structure in the steady-state sliding regime, and ζ is a measure for the structure change, which ranges from $\zeta = 0$ for the original interface to $\zeta = 1$ for the sliding regime. Since the largest amount of structure change takes place until the peak in T_t is reached, ζ can be represented as follows:

$$\begin{aligned} \text{if } T_t^s \geq T_t^{crit} : \zeta &= \frac{u_t}{u_t^s}, \text{ for } 0 \leq u_t \leq u_t^s, \\ \zeta &= 1, \text{ for } u_t > u_t^s, \\ \text{if } T_t^{crit} \geq T_t^s : \zeta &= \frac{u_t}{u_t^{crit}}, \text{ for } 0 \leq u_t \leq u_t^{crit}, \\ \zeta &= 1, \text{ for } u_t > u_t^{crit}. \end{aligned} \quad (17)$$

In Figure 12 the results from the pre-shear simulations are shown for the Fe4 interface together with the predictions by the cohesive law given by Equations 7, 16 and 17. In order to determine the parameters for the cohesive law, Equation 7 is fitted to the data of the simulations with 0 and 1000 ps pre-shear to determine ΔE for the original and the changed interface, which in turn determines T_n^{orig} and T_n^{new} . The value of ζ is determined for every amount of pre-shear with Equation 17, using the average value of u_t along the interface after the indicated pre-shear time before normal loading, and using the values of u_t^{crit} , u_t^s , T_t^{crit} and T_t^s from [9].

For various interfaces the maximum values of T_n after different pre-shear times as calculated with Equation 16 are shown in Figure 13 as the blue crosses, together with the values determined from the actual pre-shear simulations, which are given by the red dots. Predictions by the cohesive law are only shown for those interfaces for which the presence of an initial dislocation modifies the interface behaviour only very slightly, not for those interfaces where the dislocation triggers a gradual

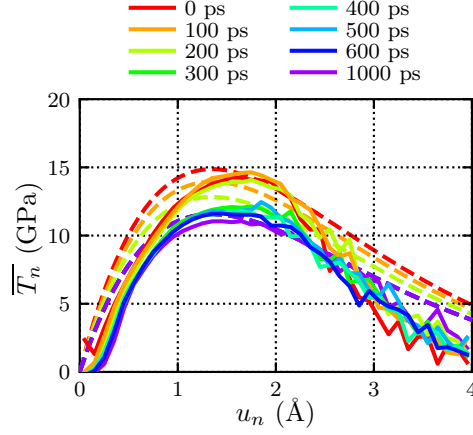


Figure 12: Normal traction as function of normal separation for the Fe4 interface under tensile loading after different amounts of applied pre-shear indicated by the different pre-shear times (solid lines), and as predicted by the cohesive law, Equations 7, 16 and 17 (dashed lines).

structure change along the interface, leading to significantly different behaviour of the changed part of the interface, as described in [9]. T_n^{orig} , T_n^{new} and ζ are determined as described above for the Fe4 interface. As can be seen in Figure 13, Equation 16 quite well reproduces \overline{T}_n^{max} from the simulations.

For the S2, X1, X2, and X3 interfaces shearing of the interface leads to a gradual structure change along the interface from the dislocation onwards, instead of to a gradual structure change of the entire interface over time as is seen for the other interfaces. In the same way as in the previously derived cohesive law [9], the gradual structure change should be included in the normal cohesive law by the factor

$$\xi = \frac{A_{new}}{A_{orig} + A_{new}}, \quad (18)$$

where A_{orig} is the area of the interface with the original structure and A_{new} is the area of the interface with the changed structure. The overall cohesive law for the entire interface is then given by

$$T_n = (1 - \xi)T_n^{orig} + \xi T_n^{new}, \quad (19)$$

where again T_n^{orig} is $T_n(u_n)$ for the original interface structure, and T_n^{new} is $T_n(u_n)$ for the part of the interface with the changed structure.

4.2. Pre-tension

Under pre-tension loading conditions the tensile load leads to an increase in u_n , which in turn may lead to a decrease in \overline{T}_t . The influence of u_n on $T_t(u_t)$ can

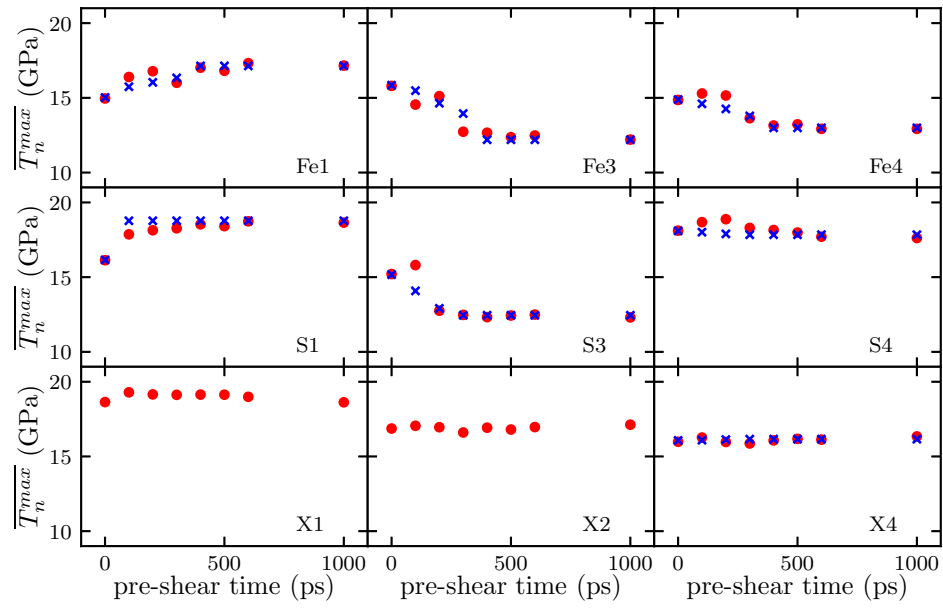


Figure 13: Average maximum normal traction during normal loading after different amounts of pre-shear are applied, indicated by the pre-shear time, for nine different interfaces (red dots). The blue crosses indicate T_n^{max} as predicted by Equation 16.

be taken into account in a similar manner as u_t in the relation for $T_n(u_n)$,

$$T_t = (1 - \eta)T_t^{orig} + \eta T_t^{new}, \quad (20)$$

where T_t^{orig} is the original relation for $T_t(u_t)$ so without a normal load being applied, and T_t^{new} is the new relation for $T_t(u_t)$ that exists if u_n reaches its critical value u_n^{crit} at which decohesion takes place. However, upon decohesion there is no contact between the surfaces at the interface and therefore $T_t^{new} = 0$. The influence of u_n on the tangential behaviour is reflected in η , which ranges from $\eta = 0$ without normal load to $\eta = 1$ upon decohesion. We define η as the fraction of u_n^{crit} that u_n has reached,

$$\eta = \frac{u_n}{u_n^{crit}}, \text{ for } 0 \leq u_n \leq u_n^{crit}. \quad (21)$$

In Figure 14 the results from pre-tension simulations are shown for the Fe4 interface together with the predictions by the cohesive law given by Equations 8, 20 and 21. For every amount of applied pre-tension η is calculated with Equation 21 by using the average value of u_n along the interface after the indicated pre-tension time before shear loading. The cohesive law for pure normal loading, Equation 7, gives $u_n^{crit} = 1.35\text{\AA}$.

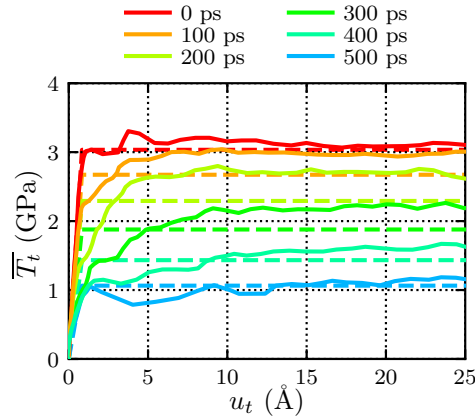


Figure 14: Tangential traction as function of tangential separation for the Fe4 interface under tensile loading after different amounts of pre-tension are applied, indicated by the different pre-tension times (solid lines), and as predicted by the cohesive law, Equations 8, 20 and 21 (dashed lines).

4.3. Mixed-mode

Under mixed-mode loading the structure change of the interface can be different from that under pre-shear or pre-tension loading conditions, as was illustrated in

Figure 11. Equation 16 for pre-shear loading assumes that once the steady-state sliding regime is reached a new interface structure is formed, which no longer changes. If under mixed-mode loading the structure change is different from that under pre-shear loading for a particular interface, T_n^{new} in Equation 16 is no longer a constant value for this interface, since for every mode-mixity angle a different structure and therefore a different T_n^{new} results. The next paragraphs describe for every interface how T_n^{new} is determined. In Table A.3 the parameters for the cohesive laws for all the interfaces are given.

For interfaces Fe3, Fe4 and S3 T_n^{new} can be considered to be a constant. The structure changes during pre-shear and mixed-mode loading are quite comparable and, as illustrated in Figure 9 for the Fe4 interface, unique relations for $T_n(u_n, u_t)$ and $T_t(u_n, u_t)$ are found.

For interfaces S4 and X4 the structure change is different for pre-shear and mixed-mode loading and, as illustrated in Figure 10 for the S4 interface, no unique relations for $T_n(u_n, u_t)$ and $T_t(u_n, u_t)$ can be found. T_n^{new} is not constant for these interfaces, but ranges between T_n^{orig} and T_n^{new} as found with a mode-mixity angle of 85° , which is the largest mode-mixity angle studied at which decohesion occurs.

Also for interface S1 the structure change is different for pre-shear and mixed-mode loading and no unique relation for $T_n(u_n, u_t)$ and $T_t(u_n, u_t)$ can be found. For this interface T_n^{new} ranges between T_n^{new} in the steady-state sliding regime and T_n^{new} as found with a mode-mixity angle of 85° . In the steady-state sliding regime and under pre-shear loading conditions $T_n(u_n)$ increases, while under mixed-mode loading $T_n(u_n)$ decreases.

For interfaces X1 and X2 the dislocation at the interface causes a gradual structure change along the interface under an applied shear load. The rate at which this structure change proceeds is dependent on the sliding velocity of the upper crystal with respect to the lower crystal, as shown in [9], and therefore on the applied shear strain rate, which for mixed-mode loading is dependent on the mode-mixity angle. Furthermore, under mixed-mode loading the 'unchanged' part of the interface shows a different response for larger mode-mixity angles. For these two interfaces, as can be seen in Figure 6, an applied pre-shear up to 1000 ps has only a small influence on $\overline{T_n^{max}}$, since it is averaged over the entire interface and only a small part of the interface shows a structure change. For a large mode-mixity angle, however, the structure change is spread much more along the interface, since in this case the applied shear strain is larger. This leads to a decrease in $\overline{T_n^{max}}$. For these interfaces T_n^{new} as found with a mode-mixity angle of 85° can be used.

The cohesive laws for normal and shear loading, Equations 7 and 8, and the modifications to include the influence of shear, respectively tension, in pre-shear and pre-tension simulations, Equations 16-21, with the parameters given in Table A.3 describe the behaviour of the interfaces studied in this work. To describe the

interface behaviour of other interfaces the parameters of the cohesive laws have to be determined. For this only a limited number of MD simulations are needed per interface and per loading direction:

- A static simulation to determine ΔE as described in [19].
- A shear simulation without initial dislocations to determine u_t^{crit} , u_t^s , T_t^{crit} , and T_t^s as described in [9].
- A tensile simulation on the interface structure formed in the steady-state sliding regime to determine T_n^{new} .
- A mixed-mode simulation with a mode-mixity angle of 85° to determine T_n^{new} if the mixed-mode behaviour is different from the pre-shear behaviour and a range has to be found in which T_n^{new} varies.
- A shear simulation with an initial dislocation to verify if this dislocation causes a gradual structure change of the interface from the dislocation position onwards. If so, \dot{A}_{new} can be determined from this simulation, and a normal simulation for this changed interface has to be performed to determine T_n^{new} .

5. Discussion

In [19] it was found that the cohesive law for normal loading can be determined based on an adhesive energy relation, Equation 7. The only factor differentiating the different interfaces was ΔE , the depth of the energy well, Equation 5. The scaling factor c was determined as an average of the scaling factors for the individual interfaces, which in turn were averages of the different simulations with different numbers of dislocations impinging on the interface. For some individual interfaces the simulation results showed small deviations from this universal normal cohesive law.

In our pre-shear simulations the value of ΔE for the changed interface in the steady-state sliding regime is not known beforehand. Instead, this value must be determined by fitting the maximum value of T_n to the normal cohesive law. Similarly, for improved accuracy for a particular interface, the maximum value of T_n from a pure normal simulation can be fitted to the cohesive law to determine ΔE . Of course, in this case not the real ΔE is found but an adjusted ΔE that includes the over- or undershoot of c for this interface.

Figures 9 and 10 clearly show that there is not a unique relation between the separations at the interface and the tractions for every interface. To properly describe the interface behaviour, no potential-based cohesive zone model can be applied if there is no unique relation. Previous studies [4, 7] based on analytical

derivations have already shown that a potential-based cohesive zone model is not capable to accurately describe interface behaviour. In this study, based on atomic-scale dynamics, we also find this. The interface structure and the change of this structure play key roles in the response to a load. To correctly capture the interface behaviour in a cohesive zone model, the structure change should therefore be included. Since the structure change depends on the order of applying shear and tensile loading, and a steady-state sliding regime can be reached, this structure change cannot be incorporated in a potential-based cohesive law.

The most commonly implemented cohesive zone model [3] has a non-periodic tangential response and therefore allows for shear failure. The cohesive law for pure shear behaviour derived in [9] is also non-periodic. However, with this cohesive law shear failure under pure shear loading will never occur, since a steady-state sliding regime is reached. Since our simulations, in [19, 9] and in the present study, involve the study of a periodic bi-crystal, the simulation set-up makes shear failure impossible.

In this study the focus is only on interface behaviour during loading and not during unloading. Since the relation between tractions and separations at the interfaces is dependent on the structure change, which in turn is determined by the loading path, it is impossible to predict the unloading behaviour of the interfaces with the currently derived cohesive model. Further study is necessary to capture the unloading behaviour.

In this study only a dislocation of the $\{112\}\langle 111 \rangle$ slip system interacts with the interface. Since the dislocation interacts with the interface under an angle, it can be expected that a different structure change will result for a dislocation of the same slip system but under a different angle, and that therefore the interface behaviour will be different. Similarly, a dislocation of another slip system will very likely cause a different structure change at the interface and therefore have a different influence on the shearing behaviour.

Before a crack grows in our simulations, it first has to nucleate. In [19] it was shown that under normal loading the crack *nucleation* behaviour is influenced by impinging dislocations, while the crack *growth* behaviour is not. In that work the crack nucleation was excluded from the determination of the crack growth behaviour. As explained in section 2.3, to determine T_t and u_t the interface is divided into bins at the beginning of the simulations, while to determine T_n and u_n this division is made every time step when these values are calculated. When, under an applied shear load, the upper crystal starts sliding with respect to the lower crystal, the upper and lower parts of the bins move apart. If then a crack forms, under a subsequently or simultaneously applied tensile load, it is not evident which bins to exclude from the analysis of the growth behaviour in order to separate the nucleation behaviour. We therefore chose in this work not to exclude the

nucleation behaviour in the determination of the crack growth behaviour. Since there are at least 175 bins along every interface, the error made by not excluding the nucleation behaviour in the crack growth behaviour is quite small. The crack nucleation behaviour itself will be discussed in a separate work [31].

In [19] and [9] the interface behaviour was studied with and without dislocations under tensile and shear loading. It was found that under tensile loading dislocations only influence the nucleation behaviour, while under shear loading, for some interfaces, dislocations in combination with the shear load cause a gradual change of the interface structure from the dislocation position onwards. In the current work all simulations are performed with an initial dislocation present at the interface, in order to trigger crack nucleation at a specific point instead of at a number of random positions. In those cases where the dislocation causes a gradual structure change of the interface, this is taken into account in the cohesive law by Equations 18 and 19.

6. Conclusions

In this work we studied the behaviour of 11 different interfaces under a shear load followed by tensile loading ('pre-shear'), a tensile load followed by shear loading ('pre-tension'), and under simultaneously applied shear and tensile loading, ('mixed-mode loading'). We find that the interface structure and the change in this structure during loading play key roles in the response to the loading. This structure change is influenced by the loading history and by the loading direction. This leads to the overall conclusion that the details of the responses of various interfaces to various loading sequences are too complex to be captured in a relatively simple scheme, see also Table 2.

Only a few general conclusions emerge:

- if a shear load changes the structure of an interface, the response to a subsequent tensile load will be different from that of the original unchanged interface,
- if under an applied shear load a barrier has to be overcome to commence sliding, first applying a tensile load will make it easier to shear the system,
- if a previously applied shear load makes it harder to obtain decohesion in the system during tensile loading, applying a shear and tensile load simultaneously will reduce this effect, since the tensile load makes shearing easier.

We have adjusted our previously derived cohesive laws for pure normal and pure shear loading [19, 9] to take into account the influence of an earlier or simultaneously applied different loading direction. For some of the interfaces a unique

relation between traction and separation exists. For other interfaces, however, no unique relation exists and our cohesive law gives no exact prediction but rather a range of possible values. This in itself is not without merit for modelling, since random values within this range can be assigned to different interfaces of the same type in a polycrystalline model. For computational practice we find that for every iron-precipitate interface a maximum of five MD simulations are needed to obtain the parameters of the cohesive zone model and to be able to fully predict the traction-separation behaviour in larger-scale models than MD.

7. Acknowledgement

This research was carried out under project number F22.2.13518b in the framework of the Partnership Program of the Materials Innovation Institute M2i and the Foundation of Fundamental Research on Matter (FOM), which is part of the Netherlands Organisation for Scientific Research (NWO). We are grateful to Erik van der Giessen and Tarun Katiyar for helpful discussions.

Appendix A. Parameters

Table A.3: Parameters for the cohesive laws given in Equations 7, 8, 16, 19, and 20. Values for ΔE are in eV, values for u_t^{crit} and u_t^s are in Å, values for T_t^{crit} , T_t^s , T_n^{orig} , and T_n^{new} are in GPa. If only T_n^{new} for steady-state sliding is given, this is the actual value for T_n^{new} . If only T_n^{new} for a mode-mixity angle of 85° is given, this indicates a range, the actual value varying between this value and T_n^{orig} , depending on the loading mode, as described in section 4.3. Where two values for T_n^{new} are given, the actual value varies between the two. For the Fe1, S2, and X3 interface no values are given for various reasons as explained in the main text.

Interface	ΔE	u_t^{crit}	u_t^s	T_t^{crit}	T_t^s	T_n^{orig}	T_n^{new}	
							steady-state sliding	mode-mixity angle 85°
Fe1	0.0519	8.08	143.35	2.92	1.95	14.96	-	-
Fe3	0.0574	2.36	132.67	3.56	2.99	15.80	12.21	-
Fe4	0.0570	0.83	0.83	3.03	3.03	14.86	12.92	-
S1	0.0519	0.69	82.26	0.86	0.34	16.13	18.65	16.29
S2	0.0686	0.15	2.72	1.24	0.92	18.23	-	-
S3	0.0530	3.72	5.16	2.71	2.47	15.21	12.31	-
S4	0.0606	1.92	6.64	3.08	2.96	18.11	-	14.35
X1	0.0601	0.14	0.14	0.02	0.02	18.64	-	16.63
X2	0.0559	0.38	0.38	0.19	0.19	16.87	-	14.95
X3	0.0755	0.00	0.00	0.01	0.01	23.73	-	-
X4	0.0555	2.19	8.17	0.96	1.67	15.99	-	15.46

References

- [1] G. I. Barenblatt, “The Mathematical Theory of Equilibrium Cracks in Brittle Fracture,” *Advances in Applied Mechanics*, vol. 7, pp. 55–129, 1962.
- [2] D. Dugdale, “Yielding of steel sheets containing slits,” *Journal of the Mechanics and Physics of Solids*, vol. 8, no. 2, pp. 100–104, 1960.
- [3] X. P. Xu and A. Needleman, “Void nucleation by inclusion debonding in a crystal matrix,” *Modelling and Simulation in Materials Science and Engineering*, vol. 1, no. 2, pp. 111–132, 1993.
- [4] M. J. van den Bosch, P. J. G. Schreurs, and M. G. D. Geers, “An improved description of the exponential Xu and Needleman cohesive zone law for mixed-mode decohesion,” *Engineering Fracture Mechanics*, vol. 73, no. 9, pp. 1220–1234, 2006.
- [5] J. Dollhofer, W. Beckert, B. Lauke, and K. Schneider, “Fracture mechanical characterisation of mixed-mode toughness of thermoplast/glass interfaces,” *Computational Materials Science*, vol. 19, no. 1-4, pp. 223–228, 2000.
- [6] K. Park, G. H. Paulino, and J. R. Roesler, “A unified potential-based cohesive model of mixed-mode fracture,” *Journal of the Mechanics and Physics of Solids*, vol. 57, no. 6, pp. 891–908, 2009.
- [7] J. P. McGarry, É. Ó. Máirtín, G. Parry, and G. E. Beltz, “Potential-based and non-potential-based cohesive zone formulations under mixed-mode separation and over-closure. Part I: Theoretical analysis,” *Journal of the Mechanics and Physics of Solids*, vol. 63, no. 1, pp. 336–362, 2014.
- [8] R. Dimitri, M. Trullo, L. De Lorenzis, and G. Zavarise, “Coupled cohesive zone models for mixed-mode fracture: A comparative study,” *Engineering Fracture Mechanics*, vol. 148, pp. 145–179, 2015.
- [9] A. Elzas, T. P. C. Klaver, and B. J. Thijssse, “Cohesive laws for shearing of iron / precipitate interfaces,” *Computational Materials Science*, vol. 152, pp. 417–429, 2018.
- [10] X. W. Zhou, J. A. Zimmerman, E. D. Reedy Jr., and N. R. Moody, “Molecular dynamics simulation based cohesive surface representation of mixed mode fracture,” *Mechanics of Materials*, vol. 40, no. 10, pp. 832–845, 2008.

- [11] X. W. Zhou, N. R. Moody, R. E. Jones, J. A. Zimmerman, and E. D. Reedy Jr., “Molecular-dynamics-based cohesive zone law for brittle interfacial fracture under mixed loading conditions: Effects of elastic constant mismatch,” *Acta Materialia*, 2009.
- [12] D. E. Spearot, K. I. Jacob, and D. L. McDowell, “Non-local separation constitutive laws for interfaces and their relation to nanoscale simulations,” *Mechanics of Materials*, vol. 36, no. 9, pp. 825–847, 2004.
- [13] D. E. Spearot, K. I. Jacob, D. L. McDowell, and S. J. Plimpton, “Effect of deformation path sequence on the behavior of nanoscale copper bicrystal interfaces,” *Journal of Engineering Materials and Technology*, vol. 127, no. 4, pp. 374–382, 2004.
- [14] C. R. Dandekar and Y. C. Shin, “Molecular dynamics based cohesive zone law for describing Al-SiC interface mechanics,” *Composites Part A: Applied Science and Manufacturing*, vol. 42, no. 4, pp. 355–363, 2011.
- [15] V. Yamakov, E. Saether, D. R. Phillips, and E. H. Glaessgen, “Molecular-dynamics simulation-based cohesive zone representation of intergranular fracture processes in aluminum,” *Journal of the Mechanics and Physics of Solids*, vol. 54, no. 9, pp. 1899–1928, 2006.
- [16] V. Yamakov, E. Saether, and E. H. Glaessgen, “Multiscale modeling of intergranular fracture in aluminum: Constitutive relation for interface debonding,” *Journal of Materials Science*, vol. 43, no. 23-24, pp. 7488–7494, 2008.
- [17] P. Gupta, S. Pal, and N. Yedla, “Molecular dynamics based cohesive zone modeling of Al (metal)-Cu50Zr50 (metallic glass) interfacial mechanical behavior and investigation of dissipative mechanisms,” *Materials and Design*, vol. 105, pp. 41–50, 2016.
- [18] B. Paliwal and M. Cherkaoui, “An improved atomistic simulation based mixed-mode cohesive zone law considering non-planar crack growth,” *International Journal of Solids and Structures*, vol. 50, no. 20-21, pp. 3346–3360, 2013.
- [19] A. Elzas and B. J. Thijssse, “Cohesive law describing crack growth at iron/precipitate interfaces,” *Computational Materials Science*, vol. 134, pp. 214–224, 2017.
- [20] G. J. Ackland, M. I. Mendeleev, D. J. Srolovitz, S. Han, and A. V. Barashev, “Development of an interatomic potential for phosphorus impurities in α -iron,” *Journal of Physics: Condensed Matter*, vol. 16, no. 27, p. S2629, 2004.

- [21] A. Elzas and B. J. Thijsse, “Dislocation impacts on iron/precipitate interfaces under shear loading,” *Modelling and Simulation in Materials Science and Engineering*, vol. 24, no. 8, p. 85006, 2016.
- [22] M. A. Tschopp and D. L. McDowell, “Structures and energies of Σ 3 asymmetric tilt grain boundaries in copper and aluminium,” *Philosophical Magazine*, vol. 87, no. 22, pp. 3147–3173, 2007.
- [23] “LAMMPS Molecular Dynamics Simulator.”
- [24] S. J. Plimpton, “Fast Parallel Algorithms for Short-Range Molecular Dynamics,” *Journal of Computational Physics*, vol. 117, no. 1, pp. 1–19, 1995.
- [25] W. M. Brown, P. Wang, S. J. Plimpton, and A. N. Tharrington, “Implementing Molecular Dynamics on Hybrid High Performance Computers - Short Range Forces,” *Computer Physics Communications*, vol. 182, pp. 898–911, 2011.
- [26] W. M. Brown, A. Kohlmeyer, S. J. Plimpton, and A. N. Tharrington, “Implementing Molecular Dynamics on Hybrid High Performance Computers - Particle-Particle Particle-Mesh,” *Computer Physics Communications*, vol. 183, pp. 449–459, 2012.
- [27] W. M. Brown and Y. Masako, “Implementing molecular dynamics on hybrid high performance computers Three-body potentials,” *Computer Physics Communications*, vol. 184, pp. 2785–2793, 2013.
- [28] A. Stukowski, “Visualization and analysis of atomistic simulation data with OVITO - the Open Visualization Tool,” *Modelling Simul. Mater. Sci. Eng.*, vol. 18, no. 1, p. 015012, 2009.
- [29] D. Faken and H. Jónsson, “Systematic analysis of local atomic structure combined with 3D computer graphics,” *Computational Materials Science*, vol. 2, no. 2, pp. 279–286, 1994.
- [30] H. Tsuzuki, P. S. Branicio, and J. P. Rino, “Structural characterization of deformed crystals by analysis of common atomic neighborhood,” *Computer Physics Communications*, vol. 177, pp. 518–523, sep 2007.
- [31] A. Elzas and B. J. Thijsse, “Crack nucleation at iron/precipitate interfaces in the presence of dislocations under different loading conditions,” *submitted to Engineering Fracture Mechanics*, 2018.